https://doi.org/10.3311/PPci.21550
Creative Commons Attribution

Periodica Polytechnica Civil Engineering, 67(2), pp. 505–517, 2023

Mechanical Response and Failure Characteristics of Granite under Unloading Conditions and Its Engineering Application

Chao Peng[1,2*], Yang Liu[1,2], Mingde Zhu[1,2], Kuikui Hou[1,2], Xingquan Liu[1,2], Guilin Li[1,2], Yantian Yin[1,2,3], Zhen Liu[1,2]

[1] Deep Mining Laboratory of Shandong Gold Group Co., Ltd., Laizhou 261442, China
[2] Shandong Key Laboratory of Deep-Sea and Deep-Earth Metallic Mineral Intelligent Mining, Laizhou 261442, China
[3] School of Resources and Environmental Engineering, Wuhan University of Technology, Wuhan 430070, China
[*] Corresponding author, e-mail: pengchao1@sd-gold.com

Received: 18 November 2022, Accepted: 13 January 2023, Published online: 08 February 2023

Abstract

Excavation in engineering significantly changes the initial stress state of rock, which makes rock inevitably in complex unloading conditions, thus it is of great significance to make a profound investigate of the mechanical characteristics of rock under unloading condition. This paper carried out two different stress paths including conventional triaxial compression and unloading confining pressure tests on granite specimen from Sanshandao gold mine, and systematically analyzed the strength characteristics, deformation characteristics and energy evolution laws. Results show that the brittle failure characteristic of granite under unloading confining pressure are more obvious, and the peak strength, axial deformation and other parameters are smaller than those of triaxial compression test. Especially the deformation modulus decreases with the increase of unloading confining pressure, which is no longer a constant parameter in the sense of continuum. Therefore, the unloading-induced weakening coefficient of engineering rock mass is proposed, and the relationship between the coefficient and the reduction ratio of confining pressure is quantified. Then, the unloading-induced weakening algorithm is developed in FLAC3D to simulate the stability of a deep mine stope. It is found that results of the unloading-induced weakening model are much closer to the engineering practice, which has certain theoretical and practical reference significance for the stability analysis of rock mass engineering.

Keywords

rock mechanics, unloading confining pressure, unloading-induced weakening, numerical simulation, stability analysis

1 Introduction

Rock mass is usually subjected to stress disturbance effects due to the impacts of rock engineering [1]. The redistributed stress of rock after excavation can be in loading or unloading states. However, the loading and unloading are two completely different stress paths, resulting in different mechanical response [2–6]. If the research results of loading rock mechanics are used blindly to guide the rock mass engineering mainly based on excavation and unloading without distinction, it will bring potential dangers and even cause accidents and disasters. Therefore, it is necessary to investigate the mechanical behavior of rock under unloading conditions and apply them to guide engineering practice.

Due to the research of rock mechanics has yielded fruitful results in loading conditions, more and more scholars begin to explore the unloading rock mechanics from various aspects such as failure mechanism, stress-strain curve and strength criterion. Crouch [7], Swanson and Brown [8] and others studied the influence of confining pressure reduction on rock strength through unloading confining pressure tests, and believed that the stress path has a certain influence on rock strength. Based on the concept of Griffith fracture mechanics, some scholars [9–11] found that mechanical parameters of rock under loading and unloading conditions are very different through experimental research, and the latter were more consistent with the excavation conditions. Gao et al. [12], Li et al. [13] and Wang et al. [14] and others carried out triaxial tests on the marble of the slope of Jinping Hydropower Station under the loading and unloading conditions, indicating that the deformation modulus under the unloading of confining pressure was decreased, and the lateral deformation

Cite this article as: Peng, C., Liu, Y., Zhu, M., Hou, K., Liu, X., Li, G., Yin, Y., Liu, Z. "Mechanical Response and Failure Characteristics of Granite under Unloading Conditions and Its Engineering Application", Periodica Polytechnica Civil Engineering, 67(2), pp. 505–517, 2023. https://doi.org/10.3311/PPci.21550

increased significantly; On this basis, Yao et al. [15], Li et al. [16] and Feng et al. [17] conducted loading and unloading tests with more complex paths, and the results showed that the stress path has a significant impact on the stress-strain curve, strength and deformation characteristics, and pointed out that the rock mass excavation is not a simple loading path, so the mechanical parameters obtained by loading in the laboratory are inaccurate, and the mechanical parameters measured by unloading path are more reasonable. Huang and Huang [18] and Li et al. [19] studied the mechanical characteristics of granite unloading failure under different initial unloading level from various aspects such as force, internal friction angle, lateral strain and maximum dilatancy, obtaining the evolution of the brittle failure. Cai and Kaiser [20] and Cai and Horii [21] deduced the nonlinear elastic constitutive model of jointed rock mass considering the influence of excavation disturbance by using statistical analysis, and applied it to the mechanical stability analysis of tunnel. Wu and Zhang [22] established a constitutive model that can reflect the unloading failure characteristics of rock according to define a disturbance function based on the concept theory of disturbance state.

From the perspective of energy, the stress state of rock is changed by excavation, which leads to the accumulation and release of energy, resulting in the instability and failure of surrounding rock. Xie et al. [23, 24] proposed the strength criterion of energy dissipation based on the energy mechanism of rock mass deformation and failure process, and pointed out that rock deformation and failure are the comprehensive results of energy dissipation and energy release. Many scholars have analyzed the characteristics of rock dissipation and expansion under different lithology [25, 26], different confining pressures [27], different unloading paths [28, 29], graded loading and unloading conditions [30, 31], and the relationship between energy and rock sample deformation and confining pressure. Peng et al. [32], Xi et al. [33] and Fan et al. [34] investigated the law of energy evolution and mechanism of initiation, propagation and coalescence of rock cracks by using numerical software. Meanwhile, many testing equipment, such as Nuclear Magnetic Resonance [35], Computed Tomography imaging technology [36, 37] and Scanning Electron Microscope [38] were combined with rock mechanics tests to study the whole process of the microcrack growth, propagation, penetration and failure of rock sample in unloading conditions.

In conclusion, it is of great significance to make a profound study of the mechanical properties of rock under the unloading condition. Through conventional triaxial compression and unloading confining pressure tests under different stress conditions, this paper systematically analyzes the mechanical properties and failure mechanism of rock under unloading confining pressure conditions from the perspective of strength, deformation and energy evolution laws. By analyzing the deformation characteristics, it is verified that the deformation modulus decreases with the increase of unloading confining pressure. Furthermore, the unloading-induced weakening coefficient of engineering rock mass is proposed, and the relationship between the coefficient and the reduction ratio of confining pressure is quantified. Then, the unloading-induced weakening algorithm is developed in FLAC3D to simulate the stability of a deep stope in Sanshandao Gold Mine. Through comparison, it is found that the unloading-induced weakening model is much reasonable and closer to the engineering practice, which has certain theoretical and practical reference significance for the stability analysis of rock mass engineering.

2 Introduction

2.1 Rock material and sample preparation

The granite cores were obtained from Sanshandao Gold Mine located in Shandong province China, the mining depth of which exceeds 1000 m. X-ray powder diffraction (XRD) analysis revealed that the mineral composition and content can be described as follows: plagioclase (44%), potash feldspar (20%), quartz (32%), and biotite (4%). The specimens were required to be processed into a cylindrical shape with a diameter of 50 mm and a height of 100 mm, which is in good agreement with the specimen size recommended by ISRM. Both ends of the specimens were polished to ensure the error of unevenness is less than 0.05 mm, and the parallelism of both ends is less than 0.25°. The NM-3C non-metallic ultrasonic tester was used to ensure the uniformity of the physical and mechanical properties of experimental specimens. The density and longitudinal wave velocity of the specimens are 2.6–2.8 g/cm^3 and 3.38–5.83 m/s, respectively. Through preliminary tests, the uniaxial compressive strength and tensile strength of the granite are determined as 81.85 MPa and 11.71 MPa, respectively.

Fig. 1(a) shows the ZTR-276 electro-hydraulic servo rock triaxial test system for triaxial compression tests and un-loading confining pressure tests in the Deep Mining Laboratory of Shandong Gold Group Co., Ltd. And the Granite specimens are shown in Fig. 1(b).

(a) (b)

Fig. 1 Mechanical test equipment and granite specimens: (a) ZTR-276 electro-hydraulic servo rock triaxial test system; (b) granite specimens

2.2 Test scheme and conditions

2.2.1 Triaxial compression test scheme

There are two purposes to carry out the conventional triaxial compression test. One is to analyze the mechanical characteristics of rock under loading conditions which will be used for the comparisons with the subsequent unloading confining pressure test. The other is to determine the peak stress of the specimen under different confining pressures which will provide the basis for the design of unloading test scheme. The triaxial compression tests are carried out under an increasing stress at a constant loading rate of 500 N/s. According to the results of in-situ stress measurements, the confining pressures are set as 10 MPa, 20 MPa and 30 MPa, respectively.

2.2.2 Unloading confining test scheme

According to different stress paths, the unloading confining pressures condition tests can be divided into three types as shown in Fig. 2.

Constant axial stress–unloading confining pressure path was selected to simulate the stress adjustment process of constant shear stress and reduced radial stress during the underground excavation cavern. The details about the schemes of unloading confining pressure test are as follows:

(1) The stress control with a constant loading rate of 2 MPa/min was used to apply confining pressure to a predetermined value, which were 10 MPa, 20 MPa and 30 MPa, respectively.

(2) The stress control was continued to apply the axial pressure at the rate of 500 N/s to the unloading point, where the value of stress level at unloading point should be greater than uniaxial compressive strength, and should be 70–90% of the corresponding triaxial compressive strength. In this paper, the starting point of unloading confining pressure was selected as 80% of triaxial compressive strength.

(3) Keep using stress path control to maintain the axial stress σ_1. At the same time, the confining pressure was unloaded at a speed of 0.01 MPa/s until the specimen failed.

3 Experimental results and discussion

3.1 Analysis of deformation characteristics

Fig. 3(a) is the full stress-strain curves of triaxial compression test under different confining pressures. It can be seen that the curves before the peak basically coincide. As the confining pressure increases, the yield stress, peak stress, and residual strength gradually increase indicating that increasing confining pressure has an inhibiting effect on the deformation and failure of the specimen which improves the load-bearing capacity of specimen. The post peak curves show the obvious elastic brittle characteristics and

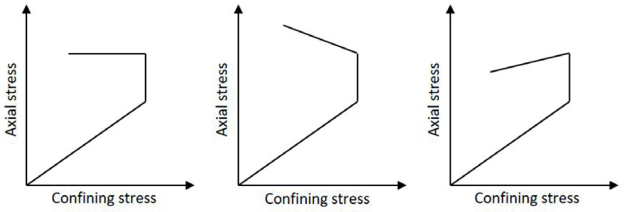

(a) (b) (c)

Fig. 2 Stress paths of unloading confining test: (a) Constant axial stress-unloading confining pressure path; (b) Adding axial stress-unloading confining pressure path; (c) Reducing axial stress-unloading confining pressure path

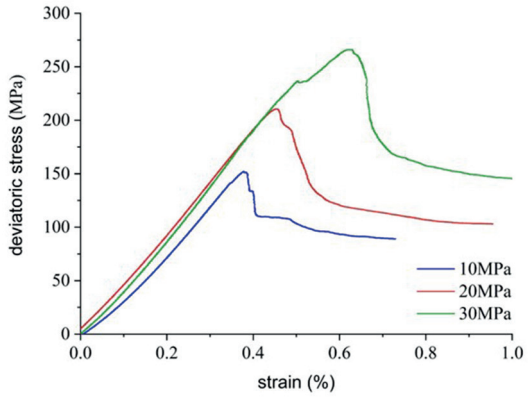

(a)

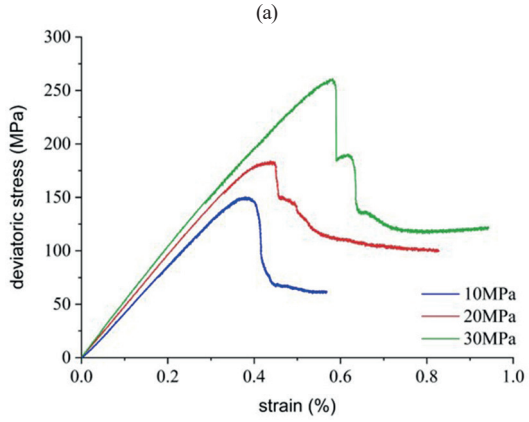

(b)

Fig. 3 Stress-strain curves of different stress paths: (a) triaxial compression test; (b) unloading confining pressure test

stress drop phenomenon. With the increase of confining pressure, the decrease of stress gradient becomes slower, and the degree of brittle failure after peak decreases.

Fig. 3(b) shows the full stress-strain curves of unloading confining test under different confining pressures. The slope of stress-strain curve before the peak is positively correlated with the confining pressure. In the unloading stage, the growth rate of deviator stress gradually increases with the confining pressure, and the rock displays a yield characteristic. With the increase of confining pressure, the process of the deviator stress decreasing to the minimum gradually becomes longer, and the specimen shows a characteristic of ductile failure.

Under the same confining pressure, the strain softening trend of granite under unloading condition is weaker than that in loading condition. Moreover, the peak strength, corresponding axial deformation to peak strength and residual strength of unloading confining pressure test are all smaller than the values of triaxial compression test, indicating that unloading condition is more likely to cause rock failure, and the brittle characteristics are more obvious.

In the unloading stage, the deformation model of rock changes to varying degrees with the increasing unloading amount, showing weakening characteristics, as show in Table 1.

3.2 Analysis of strength characteristics

The rock strength criterion can be used to characterize the relationship between stress and strength of rock materials in the critical damage condition. At present, Mohr Coulomb (M-C) criterion based on shear failure is widely used, which considers the anti-friction strength of rock is equal to the sum of the cohesion of the rock itself against shear friction and the friction force generated by the normal stress on the shear plane. M-C criterion can be expressed in the following forms,

$$\tau = c + \sigma \tan\phi\,, \tag{1}$$

$$\sigma_1 = \frac{1+\sin\phi}{1-\sin\phi}\sigma_3 + \frac{2\cos\phi}{1-\sin\phi}\,, \tag{2}$$

where τ is shear strength; σ is normal stress on shear plane; c is cohesion; φ is internal friction angle; σ_1 and σ_3 are maximum and minimum principal stress, respectively.

Fig. 4 shows the relationship between the maximum principal stress and con-fining pressure in the case of rock failure under triaxial compression test and unloading confining pressure test. The fitting expression is as follows,

$$\sigma_1 = a\sigma_3 + b\,, \tag{3}$$

where a is an influence coefficient of confining pressure on rock strength; b is the UCS (uniaxial compressive strength) obtained by fitting. Combining Eq. (2) and Eq. (3), the cohesion and internal friction angle under triaxial compression and unloading confining pressure can be obtained as follows,

$$c = b(1-\sin\phi)/(2\cos\phi)\,, \tag{4}$$

$$\phi = \arcsin[(a-1)/(a+1)]\,. \tag{5}$$

Table 1 Mechanical parameters of granite under different stress paths

Confining pressure/ MPa	Triaxial compression test		Unloading confining pressure test	
	Peak stress /MPa	Deformation modulus/GPa	Peak stress /MPa	Deformation modulus/GPa
10	162.202	44.629	157.126	41.884
20	216.57	47.776	199.157	43.712
30	296.17	48.066	285.758	47.214

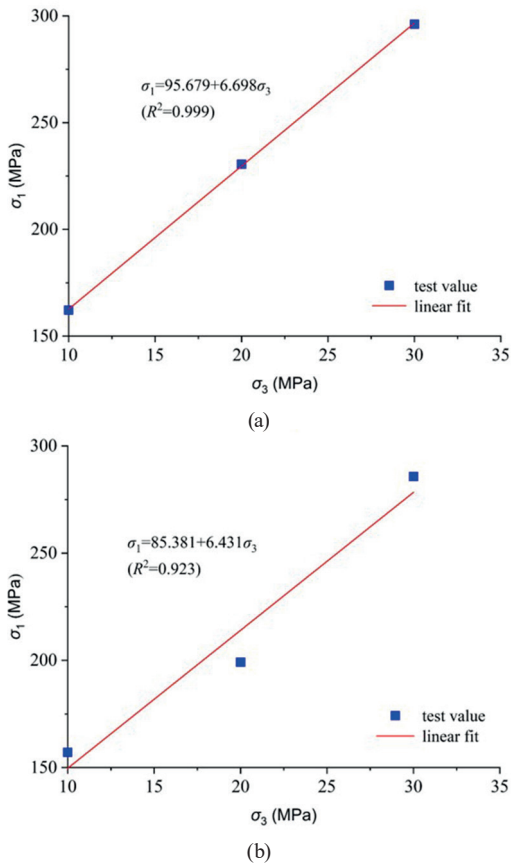

Fig. 4 Relationship between maximum principal stress and confining pressure: (a) triaxial compression test; (b) unloading confining pressure test

All the values of strength parameters under unloading confining pressure test are less than those under triaxial compression test, as show in Table 2. The values of fitting UCS, cohesion and internal friction angle are fallen by 10.763%, 7.552% and 1.656%, respectively. Furthermore, the reduction of cohesion is larger than the internal friction angle, which indicates that the stress path of unloading confining pressure mainly affects the strength of rock by reducing the cohesion.

3.3 Analysis of energy evolution

The failure process of rock is driven by energy activities, which includes energy absorption, evolution, release and dissipation of strain energy. Therefore, the failure characteristics of rock can be well described from the perspective of energy. Research shows that different types of energy accumulation during excavation correspond to different types of rock failure. A large amount of elastic energy storage can often induce rock burst, while the increase of dissipated energy will easily lead to rock spalling. As a result, more attention should be paid to judge whether the energy is accumulated in the surrounding rock, so as to avoid the damage of surrounding rock under unloading conditions. Then, reasonable excavation methods and support schemes are designed according to the energy evolution caused by unloading confining pressure.

3.3.1 Energy calculation method

In the triaxial compression test, specimen is compressed in axial direction and expanded in radial direction, so the test machine does positive work on the specimen in the axial direction, and the confining pressure caused by the expansion does negative work in radial direction. Therefore, the strain energy in the whole process can be expressed as,

$$U = U_1 + U_3, \tag{6}$$

where U is the strain energy; U_1 is the strain energy absorbed by specimen; U_3 is the strain energy consumed by the specimen.

The absorbed and consumed strain energy (U_1 and U_3) at any time during the test can be obtained by integrating the stress-strain curve with the following equations,

$$U_1 = \int_0^{\varepsilon_1^t} \sigma_1 d\varepsilon_1, \tag{7}$$

$$U_3 = 2\int_0^{\varepsilon_3^t} \sigma_3 d\varepsilon_3, \tag{8}$$

where ε_1^t and ε_3^t are the axial strain and radial strain at t time, respectively.

Table 2 Granite strength parameters

Stress path	a	b/MPa	c/MPa	φ/(°)
Triaxial compression	6.698	95.679	12.428	47.749
Unloading confining pressure	6.431	85.381	11.490	46.958

In addition, strain energy can be divided into two types: one is the elastic strain energy (U_e) stored in specimen, the other is the plastic strain energy (U_d) causing plastic deformation and crack propagation of specimen. The elastic strain energy (U_e) at any time during the test can be calculated by the following equation,

$$U = U_e + U_d, \tag{9}$$

$$U_e = \frac{1}{2E_u^t}\left[\sigma_{1t}^2 + 2\sigma_{3t}^2 - 2\mu_u^t\left(2\sigma_{1t}\sigma_{3t} + \sigma_{3t}^2\right)\right], \tag{10}$$

where $E_u{}^t$ and $\mu_u{}^t$ are the elastic modulus and Poisson's ratio at t time, respectively.

3.3.2 Energy evolution law of unloading confining pressure test

Fig. 5 shows the evolution curve of different types of energy with axial strain during unloading confining pressure test.

In the initial stage, the total energy U, dissipated energy U_d and elastic strain energy U_e increase linearly with the increase of axial stress. However, the increase of energy is small, and the values of three different types of energy are very close.

In the elastic deformation stage, the dissipated energy U_d gradually increases with the increase of axial deformation. The continuous action of the axial stress in this stage causes the internal microcracks initiate and gradually expand. The dissipated energy mainly acts on the crack growth and the friction generated by the dislocation of the crack plane. At the same time, the lateral deformation of rock specimens gradually increases, and part of the energy consumed is also used to overcome the confining pressure. The dissipated energy mainly acts on the crack propagation and the friction caused by the dislocation of the crack surface. At the same time, the transverse deformation of the specimen increases gradually, and part of the energy consumed is also used to overcome the confining pressure.

In the unloading confining pressure stage, the three types of energy continue to increase with the loading time, and the increase rate is obviously higher than that of the previous stage. The rate of increase of the dissipated energy U_d and total energy U is significantly higher than

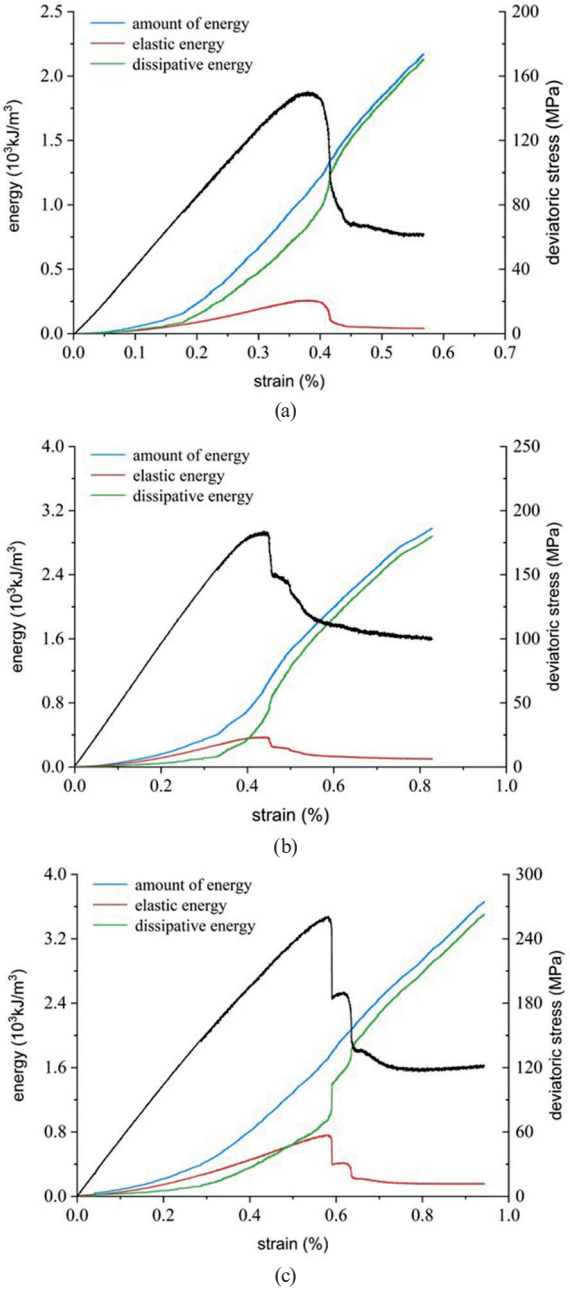

Fig. 5 Energy evolution curve of unloading confining pressure test: (a) 10 MPa; (b) 20 MPa; (c) 30 MPa

that of the previous stage, but the amplitude of increase of absorbed total energy is still greater than that of consumed energy. However, the increase of total energy is still greater than that of dissipated energy.

When the stored elastic energy reaches the maximum surface energy borne by the microscopic element of rock specimen, most of the stored elastic energy will be released rapidly, and the internal cracks of the rock specimen will converge and coalesce, eventually forming a large macroscopic fracture surface, which will lead to the failure and instability of the rock specimen in a short time.

3.3.3 energy conversion of unloading confining pressure test

To accurately reflect the energy characteristics of rock specimen under different unloading confining pressure rates, the energy increment difference (ΔU) between the starting point and the peak stress of unloading confining pressure is defined as follows,

$$\Delta U = U_{peak\ stress} - U_{unloading\ point}\ . \tag{11}$$

Meanwhile, the transformation rate ($V_{\Delta U}$) of rock strain energy before peak stress can be expressed as

$$V_{\Delta U} = \Delta U / \Delta t\ . \tag{12}$$

The energy increment of granite specimen under different unloading confining pressure conditions is shown in Fig. 6. It can be seen from the figure that the elastic strain energy increment (ΔU_e), dissipated energy increment (ΔU_d) and total energy (ΔU) increase along with the increasing of confining pressure. In addition, ΔU_d is significantly greater than ΔU_e, indicating that the energy absorbed by the specimen during the unloading confining pressure is mainly converted into the energy consumed by crack propagation, penetration and friction.

Fig. 7 shows the relationship between the pre-peak conversion rate of elastic energy U_e, dissipated energy U_d and total energy U and the initial confining pressure. The three types of energy are positively correlated with the initial confining pressure. When the initial confining pressure is 30 MPa, the energy conversion rates of U_e, U_d and U are 3.639 times, 1.572 times and 1.950 times of those when the initial confining pressure is 10 MPa, respectively, indicating that the initial confining pressure has a great influence on the crack initiation and propagation in the specimen.

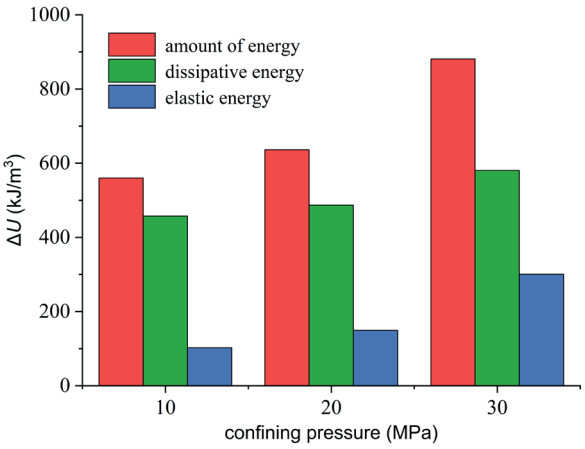

Fig. 6 Energy increment of the unloading stage under different confining pressures

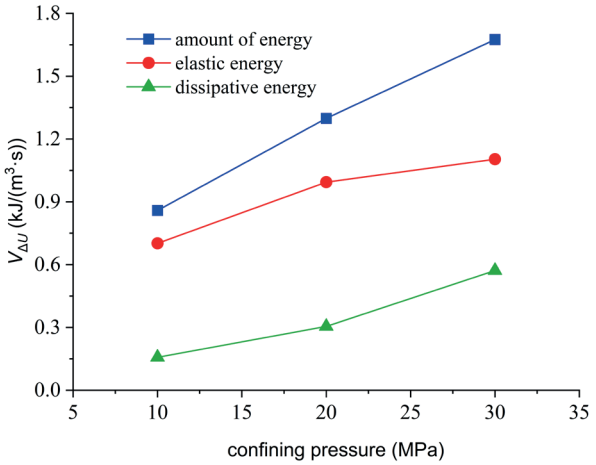

Fig. 7 Relation curve between energy conversion rate and confining pressure before peak value

Through the above analysis, the law of energy evolution in each stage of the unloading confining pressure test can be obtained. In pre-peak stage, the energy of the specimen mainly exists in the form of elastic energy and dissipated energy. In the post peak stage, the dissipated energy increases sharply, which promotes the initiation and propagation of the internal cracks and decreases the bearing capacity of the specimen, resulting in instability and fracture of the specimen.

4 Unloading-induced weakening effect and Stope stability analysis

4.1 Mechanism and significance of unloading-induced weakening effect

The excavation breaks the original stress balance of rock mass, resulting in stress redistribution, as shown in Fig. 8. As a special geological engineering material, the mechanical parameters of rock mass change with the stress environment. And the change process is mostly irreversible deterioration process. Research shows that the deformation modulus is not constant but weakened in different degree during excavation.

According to different strength characteristics after yield stress, there are four commonly used constitutive models, namely ideal elastic brittle model, strain softening model, ideal elastic plastic model and strain hardening model, as shown in Fig. 9. In the numerical simulation of geotechnical engineering, ideal elastic-plastic model and strain softening model are mostly used.

However, the weakening of mechanical parameters of rock mass during excavation is not fully reflected in these two models. The parameters in Mohr-Coulomb model are constants, and the strain softening model only considers

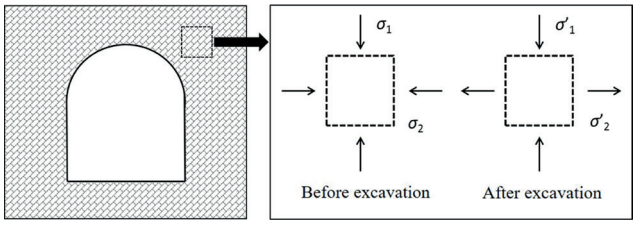

Fig. 8 Schematic diagram of excavation unloading

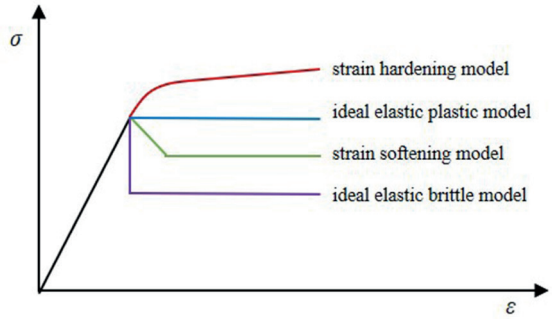

Fig. 9 Stress strain curve relationship of four common models

the weakening of cohesion and internal friction angle, and does not involve the deformation modulus. Therefore, it is of great significance for numerical calculation to consider the dynamic deterioration process of deformation modulus during excavation.

4.2 Quantitative calculation and realization of unloading induced deterioration

The deformation model is generally obtained from the stress-strain curve under uniaxial compression test, expressed as a ratio of stress σ and strain ε.

$$E = \sigma / \varepsilon \text{ or } E = d_\sigma / d_\varepsilon \tag{13}$$

As the axial strain is very small in the unloading confining pressure test, if the uniaxial stress-strain curve method is still used to calculate the deformation modulus, the results are not in accordance with the reality. It is assumed that the rock obeys the generalized Hooke's law under triaxial stress, so stress-strain relationship conforms to Eq. (14).

$$\begin{aligned} \varepsilon_1 &= \sigma_1 - \mu(\sigma_2 + \sigma_3)/E \\ \varepsilon_2 &= \sigma_2 - \mu(\sigma_1 + \sigma_3)/E \\ \varepsilon_3 &= \sigma_3 - \mu(\sigma_1 + \sigma_2)/E \end{aligned} \tag{14}$$

In the normal three-axis state, $\sigma_2 = \sigma_3$. The calculation equation of rock deformation modulus can be obtained.

$$\begin{aligned} E &= (\sigma_1 + 2\mu\sigma_3)/\varepsilon_1 \\ \mu &= (B\sigma_1 - \sigma_3)/[\sigma_3(2B-1) - \sigma_1] \\ B &= \varepsilon_3/\varepsilon_1 \end{aligned} \tag{15}$$

Combined with previously unloading confining pressure tests, the curve of deformation modulus changing with confining pressure can be obtained, as shown in Fig. 10. The horizontal axis is the percentage change of confining pressure that represents the level of stress reduction.

$$P = \frac{\sigma_3^{\ 0} - \sigma_3}{\sigma_3^{\ 0}} \times 100\%, \tag{16}$$

where P is the percentage change of confining pressure; $\sigma_3^{\ 0}$ is initial confining pressure; σ_3 is real-time confining pressure.

In order to quantify the change of deformation modulus, the unloading-induced weakening coefficient A is defined,

$$A = E / E_0, \tag{17}$$

where E is deformation modulus after weakening; E_0 is deformation modulus.

The quantitative relationship between coefficient A and percentage change of confining pressure is obtained by fitting the curve.

$$\begin{aligned} A_{10} &= 0.9988 - 0.8710P + 1.3546P^2 - 0.5290P^3 + 1.0633P^4 \quad (R^2 = 0.9976) \\ A_{20} &= 0.9871 - 0.3450P - 1.6819P^2 + 5.9938P^3 - 5.1067P^4 \quad (R^2 = 0.9962) \\ A_{30} &= 0.9816 + 0.3721P - 5.6269P^2 + 13.189P^3 - 9.0165P^4 \quad (R^2 = 0.9913) \end{aligned} \tag{18}$$

where A_{10}, A_{20} and A_{30} are the coefficient when initial stress is 10 MPa, 20 MPa and 30 MPa, respectively.

In this paper, according to the maximum principal stress, the coefficient A is selected as shown in Table 3.

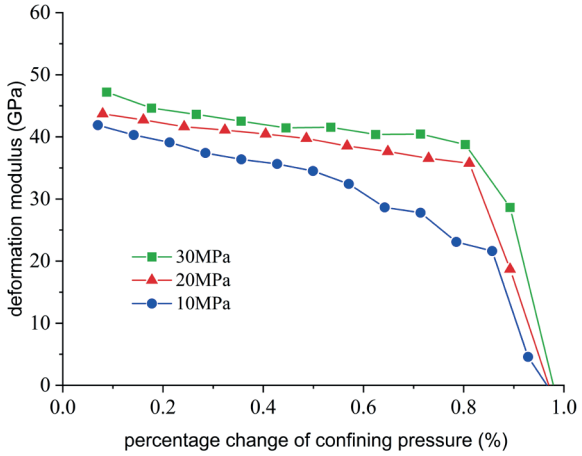

Fig. 10 Curve of deformation modulus changing with confining pressure

Table 3 Selection of stress range and coefficient

Range of stress (MPa)	<10	10–20	>20
coefficient A	A_{10}	A_{20}	A_{30}

In order to reflect the influence of excavation disturbance deterioration effect on stope stability, this paper proposed an unloading-induced weakening algorithm in numerical simulation.

The built-in strain softening model of FLAC3D is redeveloped to realize the dynamic process of deformation modulus weakened with stress reduction under excavation disturbance. Fig. 11 shows the flow chart of unloading-induced weakening algorithm. After a certain calculation steps, the horizontal principal stress situation of each unit can be judged by iterated over the model, then the corresponding coefficient according to the value of initial principal stress is selected to weak the deformation modulus. Repeat the above cycle until the simulation is completed.

4.3 Engineering case

According to the engineering geological conditions of Sanshandao Gold Mine, the numerical model from –960 m to –1005 m level is established. The model takes the extension direction of stope as X-axis, the direction perpendicular to the stope as Y-axis, and vertical direction as Z-axis. The lengths along the axis of X, Y and Z are 177 m, 40 m and 65 m, respectively. The model before excavation is composed of 94116 units and 538772 nodes, which is divided into three groups, namely, hanging wall rock group, footwall rock group and ore body group, as shown in Fig. 12.

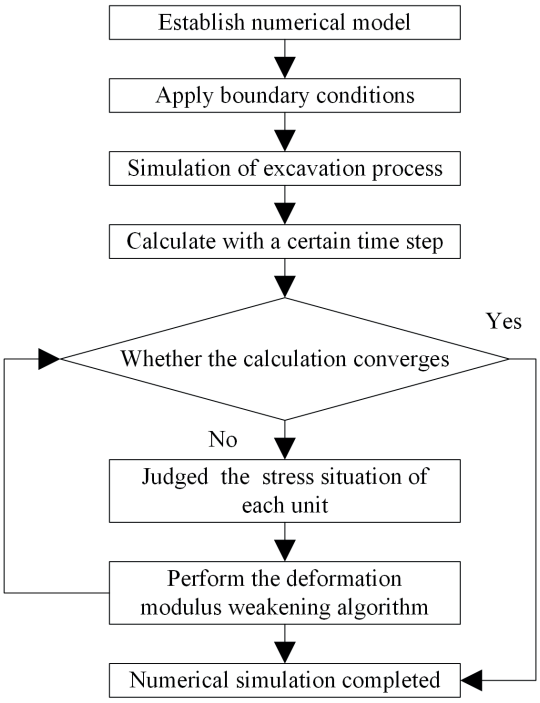

Fig. 11 The chart of unloading-induced weakening algorithm

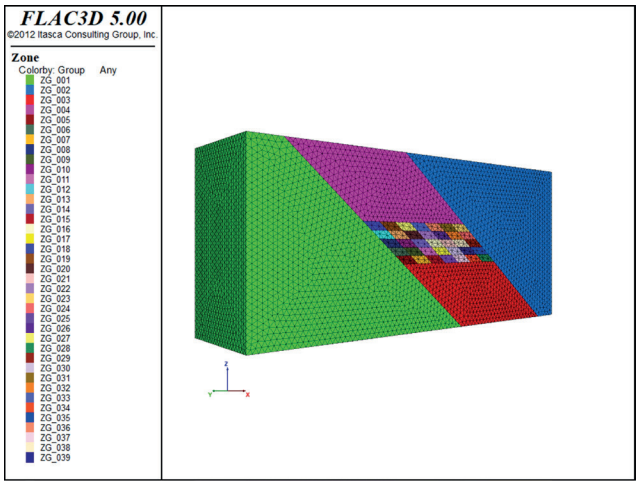

Fig. 12 3D numerical model of mine based on FLAC3D

4.3.1 Boundary condition

The stress boundary conditions are calculated according to the deep in-situ stress field model. The stresses are 33.48 MPa, 45.31 MPa and 28.59 MPa in X, Y and Z directions, respectively. Physical and mechanical parameters of rock mass are shown in Table 4.

4.3.2 Simulation results

The drift-and-fill mining stopping method is selected, taking one every the other one mining scheme with the stope span is 5 m. And the stability and failure of stope were analyzed from the perspective of deformation, stress and plastic zone.

(1) Displacement field analysis

Fig. 13 are the Z-direction displacement cloud for different excavation periods. It is observed that during the fifth step excavation, Z-direction displacement is mainly distributed over the two sides of the excavated area. Even though the filling of 1#~4# stopes has been completed, there is still large deformation on both sides of the access road. And the maximum displacement of hanging wall rock is about twice that of footwall rock. When the excavation reaches the 15th step, the maximum displacement of the goaf is transferred to roof area, reaching –72.74 mm. At this time, the surrounding rock on both sides of the 1#~10# stopes are gradually stabilized under the function of fill mass. During the 25th excavation, since both sides of 21#~25# stopes are filled, the surrounding rock displacement is small. With the excavation, the distribution range of displacement field gradually expands, but the maximum displacement is still distributed on the roof of the stope, with the value reaching 171.1 mm. At the same time, a large area of floor heave also occurs.

(2) Stress field analysis

The stress state is the most important factor affecting the stability of stope. Analyzing the change of stress field is helpful to take targeted support measures for the area with large deformation. In FLAC3D, the tensile stress is positive and the compressive stress is negative. The maximum principal stress and minimum principal stress are determined by the absolute value.

With the gradual development of mining, the maximum principal stress distribution cloud of the stope is shown in Fig. 14. At the beginning of excavation, the maximum principal stress is mainly distributed over the corner area

Table 4 Mechanical parameters of deep rock mass in Sanshandao Gold Mine

Type	Rock mass	Ore	Filling body
Density (kg/m^3)	2700	2900	2160
Cohesion (MPa)	1.29	2.83	0.84
Internal friction angle (°)	41.35	41.57	38
Tensile strength (MPa)	0.42	0.25	0.5
Compressive strength (MPa)	8.23	12.84	\
Elastic modulus (GPa)	16.00	19.13	6.1
Poisson's ratio	0.25	0.21	0.36

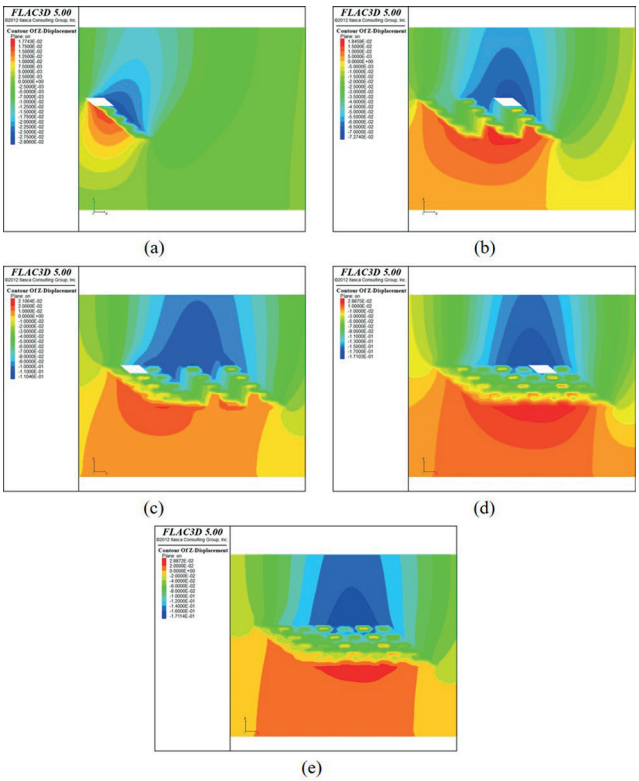

Fig. 13 Z-direction displacement cloud for different excavation periods: (a) after excavation 5 steps; (b) after excavation 15 steps; (c) after excavation 25 steps; (d) after excavation 35 steps; (e) excavation completed

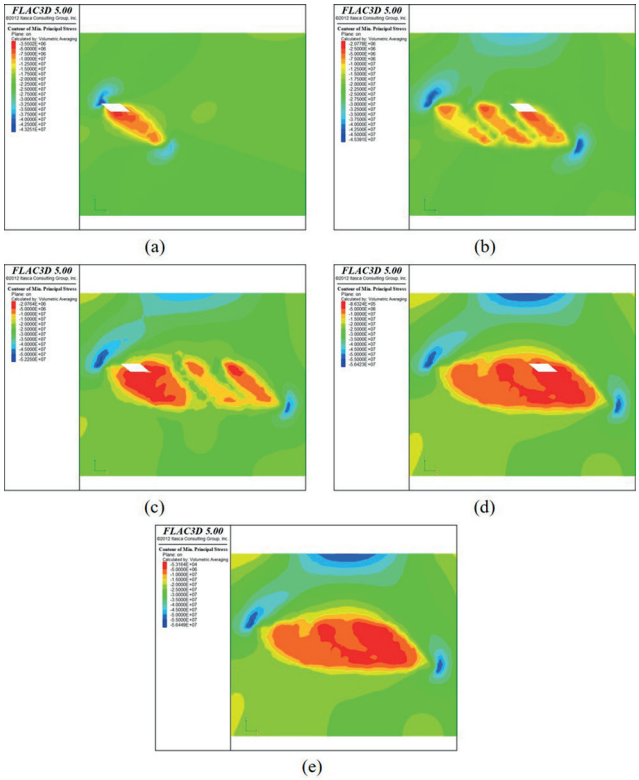

Fig. 14 Maximum principal stress cloud for different excavation periods: (a) after excavation 5 steps; (b) after excavation 15 steps; (c) after excavation 25 steps; (d) after excavation 35 steps; (e) excavation completed

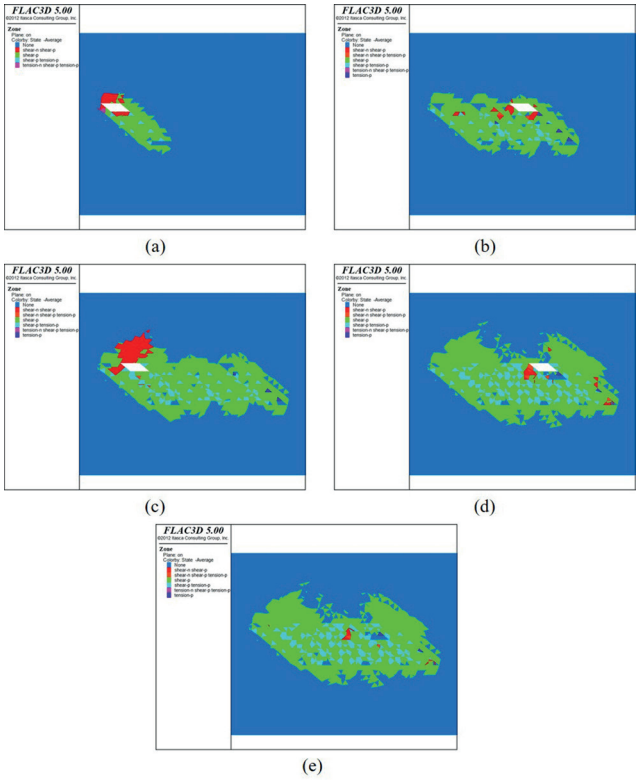

Fig 15. Maximum principal stress cloud for different excavation periods: (a) after excavation 5 steps; (b) after excavation 15 steps; (c) after excavation 25 steps; (d) after excavation 35 steps; (e) excavation completed

near the roof of the footwall rock. With the excavation, the stress of stope is released, and the maximum principal stress is always concentrated in the bottom and top corner of the stope. After excavation, the maximum principal stress reaches 56.45 MPa, but there is no tensile stress during the whole process.

(3) Plastic zone analysis

Fig. 15 show the distribution characteristics of the plastic zones at different excavation periods. During the fifth step, the plastic zone is mainly distributed in the surface area of rock around the mined stopes, mainly in shear failure. With the progress of excavation, the plastic zone is not only distributed in the surrounding rock, but also in the roof and floor of the mined stopes. It is also dominated by shear failure, accompanied by tensile failure. After excavation, the plastic zone area increases and more complex failures occur. At that time, a large area of shear failure occurs on the roof of 20# stope, but the filling bodies of 21#~35# stopes have not yet been damaged.

4.4 Comparison and verification

By comparing within the results of strain softening model and combining with the field monitoring data, the analysis is conducted from the perspective of Z-direction displacement to verify the reliability of unloading-induced weakening algorithm in stability simulation.

Since the displacement has different values depending on the position during excavation, five monitoring sites are set in the model, whose Z-direction displacement and coordinate are shown in Table 5 and Fig. 16, in order to better analyze the change of displacement. It can be seen that the strain softening model does not consider the unloading-induced effect of deformation modulus, and the displacement of which is only 0.56~0.85 times compare to that of unloading-induced weakening model, resulting in a much conservative stability evaluation.

Table 5 Coordinates and displacements of numerical monitoring sites

Monitoring site	Coordinate			Z-direction displacement/m	
	X	Y	Z	Unloading-induced weakening model	Strain softening model
1#	–6.5	20	15	0.10766	0.06563
2#	–1.5	20	15	0.13453	0.0761
3#	3.5	20	15	0.15426	0.0944
4#	8.8	20	15	0.16726	0.1254
5#	13.5	20	15	0.17113	0.1465

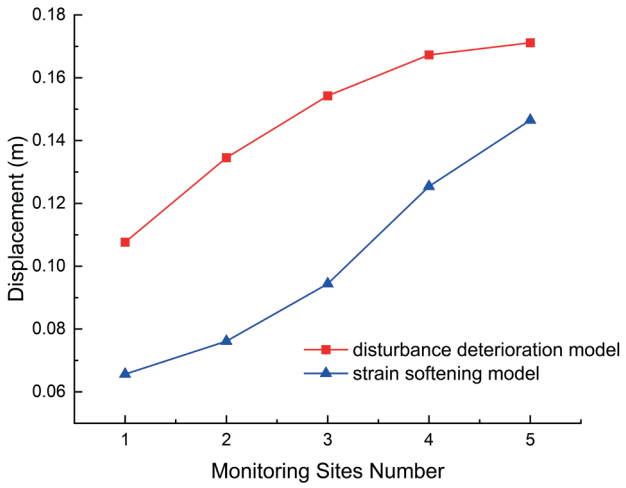

Fig. 16 Data of simulation monitoring

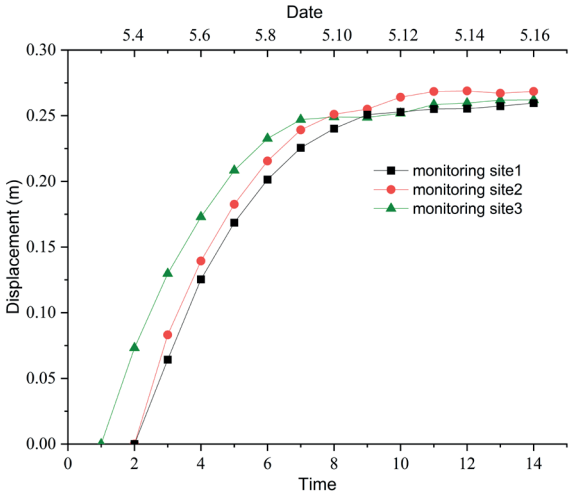

Fig. 17 Data of on-site monitoring

The convergence gauge (JSS30A) was used for on-site monitoring, and the monitoring results are shown in Fig. 17, the deformation rate of each monitoring site changed greatly in the early stage, and gradually decreases after about a week, showing a stable trend. The average vertical displacement of roof at monitoring sites 1#~3# in the monitoring period is about 25 mm. A comparison showed that the simulation result of unloading-induced weakening model is much closer to the site monitoring data, that is to say this model is more consistent with the excavation conditions.

5 Conclusions

(1) During the unloading confining pressure process, the growth rate of deviator stress gradually increases with the confining pressure. After the peak stress, the decreasing process of deviator stress is prolonged with the increase of confining pressure. Under same confining pressure, rock in the unloading confining condition has obvious brittleness characteristics, and the deviator stress, peak axial strain and residual strength are lower than those in the triaxial compression conditions.

(2) In pre-peak stage, the energy of the specimen mainly exists in the form of elastic energy and dissipated energy. In the post peak stage, the dissipated energy increases sharply, which promotes the initiation and propagation of the internal cracks and decreases the bearing capacity of the specimen, resulting in instability and fracture of the specimen.

(3) In unloading confining pressure test, the deformation modulus weakens gradually with the increase of unloading pressure, indicating that the deformation modulus has an unloading-induced weakening effect. The quantitative relationship between unloading-induced weakening coefficient A and the reduction ratio of confining pressure is obtained by analyzing the change of deformation modulus during the unloading tests, then the unloading-induced weakening model of engineering rock mass is developed in FLAC3D to simulate the stability of a deep stope. Through comparison, it is verified that the unloading-induced weakening model is much closer to the engineering practice.

(4) The simulation shows that due to the weak strength of the filling body, the rock of the stope is squeezed into the goaf under the action of stress, especially the roof and floor will have a large deformation. Therefore, the support of roof should be strengthened in order to reduce roof deformation or collapse. Furthermore, excavation will cause the release of the original stress in surrounding rock, and the maximum principal stress is always concentrated in the bottom and top corner of the stope. So, targeted support measures should be taken for the corner area when excavating the top and bottom stope.

Acknowledgement

The project presented in this article is supported by Major Basic Research Project of Shandong Province - Mechanism of mining-induced fault slip and rock burst disaster and intelligent quantitative warning (ZR2021ZD36).

References

[1] Hudson, J. A., Harrison, J. P. "Engineering Rock Mechanics: An Introduction to the Principles", Elsevier, 2000. ISBN 978-0-08-043864-1
https://doi.org/10.1016/B978-0-08-043864-1.X5000-9

[2] Cai, M. F., He, M. C., Liu, D. Y. "Rock Mechanics and Engineering", Science Press, 2002. ISBN 9787030104700

[3] Li, J. L., Wang, H. "Theories of Unloading Rock Mass Mechanics and its Engineering Practice", Science Press, 2016. ISBN 97870304 63067

[4] Li, J. L. "Unloading Rock Mass Mechanics", China Water and Power Press, 2003. ISBN 9787508416212

[5] Peng, C., Wang, J., Liu, H., Li, G., Zhao, W. "Investigating the macro-micro mechanical properties and failure law of granite under loading and unloading conditions", Advances in Civil Engineering, 2021, 9983427, 2021.
https://doi.org/10.1155/2021/9983427

[6] Huang, R. Q., Huang, D. "Evolution of rock cracks under unloading condition", Rock Mechanics and Rock Engineering, 47, pp. 453–466, 2014.
https://doi.org/10.1007/s00603-013-0429-0

[7] Crouch, S. L. "A note on post-failure stress-strain path dependence in norite", International Journal of Rock Mechanics and Mining Science and Geomechanics Abstracts, 9(2), pp. 197–204, 1972.
https://doi.org/10.1016/0148-9062(72)90022-8

[8] Swanson, S. R., Brown, W. S. "An observation of loading path independence of fracture in rock", International Journal of Rock Mechanics and Mining Science and Geomechanics Abstracts, 8(3), pp. 277–281, 1971.
https://doi.org/10.1016/0148-9062(71)90023-4

[9] Lau, J. S. O., Chandler, N. A. "Innovative laboratory testing", International Journal of Rock Mechanics and Mining Sciences, 41(8), pp. 1427–1445, 2004.
https://doi.org/10.1016/j.ijrmms.2004.09.008

[10] Trippetta, F., Collettini, C., Meredith, P. G., Vinciguerra, S. "Evolution of the elastic moduli of seismogenic Triassic Evaporites subjected to cyclic stressing", Tectonphysics, 592, pp. 67–79, 2013.
https://doi.org/10.1016/j.tecto.2013.02.011

[11] Chandler, N. A. "Quantifying long-term strength and rock damage properties from plots of shear strain versus volume strain", International Journal of Rock Mechanics and Mining Sciences, 59, pp. 105–110, 2013.
https://doi.org/10.1016/j.ijrmms.2012.12.006

[12] Gao, C. Y., Xu, J., He, P., Liu, J. F. "Study on mechanical properties of marble under loading and unloading conditions", Chinese Journal of Rock Mechanics and Engineering, 24(3), pp. 456–460, 2005. (in Chinese)
https://doi.org/10.3321/j.issn:1000-6915.2005.03.015

[13] Li, H. Z., Xia, C. C., Yan, Z. J., Jiang, K., Yang, L. D. "Study on marble unloading mechanical properties of Jinping hydropower station under high geostress conditions", Chinese Journal of Rock Mechanics and Engineering, 26(10), pp. 2104–2109, 2007. (in Chinese)
https://doi.org/10.3321/j.issn:1000-6915.2007.10.021

[14] Wang, B., Zhu, J. B., Wu, A. Q., Hu, J. M., Xiong, Z. M. "Experimental study on mechanical properties of Jinping marble under loading and unloading stress paths", Chinese Journal of Rock Mechanics and Engineering, 27(10), pp. 2138–2145, 2008. (in Chinese)
https://doi.org/10.3321/j.issn:1000-6915.2008.10.024

[15] Yao, H., Jia, S., Li, H. "Experimental study on failure characteristics of schist under unloading condition", Geotechnical and Geological Engineering, 36, pp. 905–913, 2018.
https://doi.org/10.1007/s10706-017-0364-z

[16] Li, X., Cao, W., Zhou, Z., Zou, Y. "Influence of stress path on excavation unloading response", Tunnelling and Underground Space Technology, 42, pp. 237–246, 2014.
https://doi.org/10.1016/j.tust.2014.03.002

[17] Feng, X.-T., Gao, Y., Zhang, X., Wang, Z., Zhang, Y., Han, Q. "Evolution of the mechanical and strength parameters of hard rocks in the true triaxial cyclic loading and unloading tests", International Journal of Rock Mechanics and Mining Sciences, 131, 104349, 2020.
https://doi.org/10.1016/j.ijrmms.2020.104349

[18] Huang, R. Q., Huang, D. "Experimental research on mechanical properties of granites under unloading condition", Chinese Journal of Rock Mechanics and Engineering, 27(11), pp. 2205–2213, 2008. (in Chinese)
https://doi.org/10.3321/j.issn:1000-6915.2008.11.005

[19] Li, D., Sun, Z., Xie, T., Li, X., Ranjith, P. G. "Energy evolution characteristics of hard rock during triaxial failure with different loading and unloading paths", Engineering Geology, 228, pp. 270–281, 2017.
https://doi.org/10.1016/j.enggeo.2017.08.006

[20] Cai, M., Kaiser, P. K. "Assessment of excavation damaged zone using a micromechanics model", Tunnelling and Underground Space Technology, 20(4), pp. 301–310, 2005.
https://doi.org/10.1016/j.tust.2004.12.002

[21] Cai, M., Horii, H. "A constitutive model of highly jointed rock masses", Mechanics of Materials, 13(3), pp. 217–246, 1992.
https://doi.org/10.1016/0167-6636(92)90004-W

[22] Wu, G., Zhang, L. "Studying unloading failure characteristics of a rock mass using the disturbed state concept", International Journal of Rock Mechanics and Mining Sciences, 41, 437, 2004.
https://doi.org/10.1016/j.ijrmms.2003.12.077

[23] Xie, H. P., Liu, J. F., Ju, Y., Xie, L. Z. "Fractal property of spatial distribution of acoustic emissions during the failure process of bedded rock salt", International Journal of Rock Mechanics and Mining Sciences, 48(8), pp. 1344–1351, 2011.
https://doi.org/10.1016/j.ijrmms.2011.09.014

[24] Xie, H., Li, L., Peng, R., Ju, Y. "Energy analysis and criteria for structural failure of rocks", Journal of Rock Mechanics and Geotechnical Engineering, 1(1), pp. 11–20, 2009.
https://doi.org/10.3724/SP.J.1235.2009.00011

[25] Hou, Z.-K., Cheng, H.-L., Sun, S.-W., Qi, D.-Q., Liu, Z.-B. "Crack propagation and hydraulic fracturing in different lithologies", Applied Geophysics, 16, pp. 243–251, 2019.
https://doi.org/10.1007/s11770-019-0764-3

[26] Gao, L., Gao, F., Zhang, Z., Xing, Y. "Research on the energy evolution characteristics and the failure intensity of rock", International Journal of Mining Science and Technology, 30(5), pp. 705–713, 2020. https://doi.org/10.1016/j.ijmst.2020.06.006

[27] Liu, W., Zhang, X., Li, H., Chen, J. "Investigation on the Deformation and Strength Characteristics of Rock Salt Under Different Confining Pressures", Geotechnical and Geological Engineering, 38, pp. 5703–5717, 2020. https://doi.org/10.1007/s10706-020-01388-1

[28] Zhao, Y., Bi, J., Wang, C., Liu, P. "Effect of unloading rate on the mechanical behavior and fracture characteristics of sandstones under complex triaxial stress conditions", Rock Mechanics and Rock Engineering, 54, pp. 4851–4866, 2021. https://doi.org/10.1007/s00603-021-02515-x

[29] Jia, Z., Li, C., Zhang, R., Wang, M., Gao, M., Zhang, Z., Zhang, Z., Ren, L., Xie, J. "Energy evolution of coal at different depths under unloading conditions", Rock Mechanics and Rock Engineering, 52, pp. 4637–4649, 2019. https://doi.org/10.1007/s00603-019-01856-y

[30] Zhao, G., Dai, B., Dong, L., Yang, C. "Energy conversion of rocks in process of unloading confining pressure under different unloading paths", Transactions of Nonferrous Metals Society of China, 25(5), pp. 1626–1632, 2015. https://doi.org/10.1016/S1003-6326(15)63767-0

[31] Han, C., Pang, J. D., Li, D. J. "Analysis of energy evolution during the step loading and unloading creep experiments of sandstone", Rock and Soil Mechanics, 41(4), pp. 1–10, 2020. (in Chinese) https://doi.org/10.16285/j.rsm.2019.0872

[32] Peng, C., Guo, Q., Yan, Z., Wang, M., Pan, J. "Investigating the Failure Mechanism of Jointed Rock Slopes Based on Discrete Element Method", Advances in Civil Engineering, 2020, 8820158, 2020. https://doi.org/10.1155/2020/8820158

[33] Xi, X., Wu, X., Guo, Q., Cai, M. "Experimental Investigation and Numerical Simulation on the Crack Initiation and Propagation of Rock with Pre-Existing Cracks", IEEE Access, 8, pp. 129636–129644, 2020. https://doi.org/10.1109/ACCESS.2020.3009230

[34] Fan, X; Kulatilake, P. H. S. W; Chen, X. "Mechanical behavior of rock-like jointed blocks with multi-non-persistent joints under uniaxial loading: A particle mechanics approach", Engineering Geology, 190(5), pp. 17–32, 2015. https://doi.org/10.1016/j.enggeo.2015.02.008

[35] Guo, J.-C., Zhou, H.-Y., Zeng, J., Wang, K.-J., Lai, J., Liu, Y.-X. "Advances in low-field nuclear magnetic resonance (NMR) technologies applied for characterization of pore space inside rocks: a critical review", Petroleum Science, 17, pp. 1281–1297, 2020. https://doi.org/10.1007/s12182-020-00488-0

[36] Ketcham, R. A., Carlson, W. D. "Acquisition, optimization and interpretation of X-ray computed tomographic imagery: applications to the geosciences", Computers and Geosciences, 27(4), pp. 381–400, 2001. https://doi.org/10.1016/S0098-3004(00)00116-3

[37] Berg, C. F., Lopez, O., Berland, H. "Industrial applications of digital rock technology", Journal of Petroleum Science and Engineering, 157, pp. 131–147, 2017. https://doi.org/10.1016/j.petrol.2017.06.074

[38] Erarslan, N., Williams, D. J. "The damage mechanism of rock fatigue and its relationship to the fracture toughness of rocks", International Journal of Rock Mechanics and Mining Sciences, 56, pp. 15–26, 2012. https://doi.org/10.1016/j.ijrmms.2012.07.015